Quantum cutting effect in $KY_3F_{10}:Tm^{3+}$

Léna Beauzamy* and Bernard Moine†
Laboratoire de Physico-Chimie des Matériaux Luminescents, CNRS, UMR5620, Université Lyon 1, Université de Lyon, 69622 Villeurbanne, France

Richard S. Meltzer‡ and Yi Zhou§
Department of Physics and Astronomy, University of Georgia, Athens, Georgia 30602, USA

Patrick Gredin‖
Laboratoire de Chimie de la Matière Condensée de Paris–UMR 7574, Université Pierre-et-Marie Curie, 75005 Paris, France

Anis Jouini¶ and Kyoung Jin Kim**
Fukuda Laboratory, Institute of Multidisciplinary Research for Advanced Materials, Tohoku University, Sendai 980-8576, Japan
(Received 18 July 2008; published 6 November 2008)

A cross-relaxation energy-transfer scheme using the $5d$ state of Tm^{3+} as the donor and the $4f^{13}$ states of Tm^{3+} as the acceptor is proposed. The scheme is tested in the host KY_3F_{10} doped with several concentrations of Tm^{3+} as a potential vacuum ultraviolet (VUV) excited blue phosphor of quantum yield greater than unity. Emission and diffuse reflection spectra along with studies of the time evolution of the $5d$ and $4f$ populations of Tm^{3+} in KY_3F_{10} crystals and powders under UV and VUV excitations are reported and analyzed. The results show that the proposed quantum cutting mechanism occurs but the $^1I_6$, $^1D_2$, and $^1G_4$ acceptor levels cross relax rapidly to lower-lying levels by an additional cross-relaxation energy transfer and that this effectively quenches the blue emission. Based on the temperature dependence of the spectra, an interesting heat-assisted relaxation process involving intersystem crossing is observed above 300 K.

DOI: 10.1103/PhysRevB.78.184302 PACS number(s): 78.55.Hx

I. INTRODUCTION

The use of xenon in plasma display panels and in new fluorescent lamps as a substitute for mercury necessitates phosphors capable of emitting more than one visible photon for each vacuum ultraviolet (VUV) photon absorbed. Such phosphors have a quantum yield greater than 1 and operate by a process called quantum cutting or down-conversion. This paper describes a detailed study of a phosphor capable of emitting two blue photons for each VUV photon absorbed: KY_3F_{10} (KYF):Tm^{3+}. The quantum cutting occurs by a cross-relaxation energy transfer (CRET) in a pair of Tm^{3+} ions. The quantum cutting is characterized by emission, excitation, and reflectivity measurements in the visible, UV, and VUV ranges, and is studied as a function of concentration and temperature. In the first part a rationale is given for how Tm^{3+} as dopant ion and KY_3F_{10} as host lattice where chosen. The second part describes the two different methods used to synthesize the materials. In the third part, the experimental methods are described. In the last part the results are presented, where it is shown that efficient quantum cutting is observed. However the application of this material is ultimately limited by subsequent cross relaxation of the levels giving rise to the blue emission and a thermally assisted relaxation from initially excited $5d$ state to the $4f$ levels.

II. SELECTION OF DOPANT ION AND HOST LATTICE

Because of its $^1D_2 \rightarrow {}^3F_4$, $^3P_0(^1I_6) \rightarrow {}^3H_4$, and $^1G_4 \rightarrow {}^3H_6$ blue transitions, the trivalent thulium appears to be the most interesting ion among the trivalent rare-earth (RE) ions to realize a blue phosphor. Furthermore the energy diagram of Dieke[1] shows that the energy-level scheme of Tm^{3+} is relatively simple. Indeed Tm^{3+} has only about ten levels between 0 and 40 000 cm^{-1} and the high-energy extension of the Dieke diagram[2] shows no levels between 40 000 and 70 000 cm^{-1}. Another important advantage of Tm^{3+} is that it acts as both the donor and acceptor in the CRET, thereby avoiding the introduction of a second type of dopant ion which could provide additional unwanted relaxation channels. So Tm^{3+} has been chosen because of its known blue transitions and the relative simplicity of its energy-level diagram.

The host lattice has been selected with the help of a paper by Dorenbos,[3] which presents an empirical relationship for calculating the energy of the first $4f \rightarrow 5d$ transition. The calculation presented in this paper allowed us to predict in which host the original energy-transfer scheme shown in Fig. 1 would be possible. The means to obtain quantum cutting is described by the following steps using $^1D_2$ as an example; other pathways are also possible as discussed below:

(a) Excitation of one Tm^{3+} ion by the $4f^n \rightarrow 4f^{n-1}5d$ transition, by absorption of one VUV photon (step 1). This transition involves the $5d$ "low-spin" (5dLS) band that is spin allowed since it has the same spin as the ground level.

(b) After the 5dLS band is populated, it is expected that very rapid vibrational relaxation occurs into the lowest $5d$ high-spin (5dHS) band at the lowest energy. This vibrational relaxation is in competition with direct VUV 5dLS $\rightarrow 4f$ spin-allowed emission. Furthermore, while this spin-allowed emission has been reported several times in the literature, the

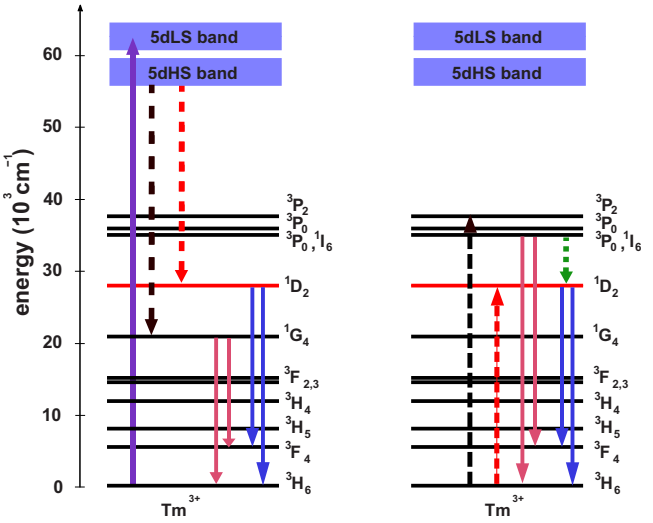

FIG. 1. (Color online) Scheme of quantum cutting mechanism involving two Tm^{3+} ions, leading to the emission of two blue photons. This is a simplified scheme of the Tm^{3+} states and possible mechanisms. The different transitions from the $^3P_J(^1I_6)$ and $^1D_2$ levels are shown only for the two first levels ($^3F_4$ and $^3H_6$).

dominant emission is the VUV 5dHS$\rightarrow 4f$ spin-forbidden emission.[4–8]

(c) After relaxation to the 5dHS band, a cross-relaxation energy-transfer process occurs involving a second Tm^{3+} ion, leaving both ions in their $^1D_2$ states (step 2). This mechanism occurs in competition with the VUV 5dHS$\rightarrow 4f$ spin-forbidden emission.

(d) Because the $^1D_2$ level is responsible for the blue $^1D_2 \rightarrow {}^3F_4$ transition, each Tm^{3+} ion can emit a blue photon, leading to the possibility of a quantum yield of 2.

The occurrence of this quantum cutting mechanism is strongly dependent on the $5d$ energy levels and therefore it depends on the host lattice. The 5dHS$\rightarrow {}^1D_2$ and $^3H_6 \rightarrow {}^1D_2$ transitions must be resonant; i.e., the energy of the VUV spin-forbidden 5dHS$\rightarrow 4f(^3H_6)$ emission must be twice the energy of the $^1D_2$ level. Using the Dorenbos relationship, the selection of the ideal host lattice is made based on the following equations:

$$E_{\text{emiHS}}(\text{Tm}^{3+},A) = 2 \times E(^1D_2), \tag{1}$$

$$E_{\text{emiHS}}(\text{Tm}^{3+},A) = E_{\text{absLS}}(\text{Tm}^{3+},A) - \Delta E^{\text{Tm}^{\text{sa}},\text{Tm}^{\text{sf}}} - \Delta\text{Stokes}(A), \tag{2}$$

$$E_{\text{absLS}}(\text{Tm}^{3+},A) = 49\,340 - D(A) + \Delta E^{\text{Tm}^{3+},\text{Ce}^{3+}}. \tag{3}$$

Noting that $\Delta E^{\text{Tm}^{3+},\text{Ce}^{3+}}$ is equal to 29 300 and substituting Eqs. (1) and (3) into Eq. (2), one obtains

$$D(A) + \Delta\text{Stokes}(A) = 20\,790. \tag{4}$$

(a) $E_{\text{emiHS}}(\text{Tm}^{3+},A)$ represents the energy of the 5dHS $\rightarrow {}^3H_6$ emission of Tm^{3+} in host lattice A.

(b) $E(^1D_2)$ is the energy of the $^1D_2$ level or the energy required for the $^3H_6 \rightarrow {}^1D_2$ transition and is 27 500 cm^{-1}.

TABLE I. $D(A)$ and $\Delta\text{Stokes}(A)$ values of KY_3F_{10} found in the paper of Dorenbos (Ref. 3).

Host lattice	$D(A)$ (cm^{-1})	$\Delta\text{Stokes}(A)$ (cm^{-1})	$D(A)+\Delta\text{Stokes}(A)$ (cm^{-1})
KY_3F_{10}	16084	3921	20005

(c) $E_{\text{absLS}}(\text{Tm}^{3+},A)$ is the energy required for the corresponding allowed transition in host lattice A.

(e) Using the notations of Dorenbos,[3] $\Delta E^{\text{Tm}^{\text{sa}},\text{Tm}^{\text{sf}}}$ (2350 cm^{-1}) represents the energy difference between the first 5dHS and 5dLS bands of Tm^{3+}, $\Delta\text{Stokes}(A)$ and $D(A)$ represent, respectively, the Stokes shift in host lattice A and the crystal field depression in host A, and $\Delta E^{\text{Tm}^{3+},\text{Ce}^{3+}}$ (29 300 cm^{-1}) represents the energy difference between the first $4f^n \rightarrow 4f^{n-1}5d(\text{LS})$ transition of Ce^{3+} and that of Tm^{3+} in the same host lattice.

Energies are expressed in cm^{-1}. The Dorenbos empirical relationship is introduced in Eq. (3). These calculations lead to a condition about host lattice A that allows one to select the right host with the help of the values of $D(A)$ and $\Delta\text{Stokes}(A)$ for many hosts given in the paper of Dorenbos.[3] Adding $D(A)$ and $\Delta\text{Stokes}(A)$ for all hosts leads to the conclusion that the best fluoride host seems to be KY_3F_{10}. The values of this host lattice match very closely the ideal values (see Table I). Quantum cutting based on CRET in a pair of Tm^{3+} (step 2 in Fig. 1) must compete effectively with the VUV-forbidden emission from the 5dHS to the ground state. Since the CRET rate is strongly dependent on concentration, it appears interesting to study materials with high Tm^{3+} concentrations so as to maximize this process. Therefore we have synthesized a series of KY_3F_{10}:Tm^{3+} powders with 0.5, 1, 2, 5, and 7% of Tm^{3+} and a series of KY_3F_{10}:Tm^{3+} crystals with 5, 10, 20, 30, 50, and 80% of Tm^{3+}.

III. SYNTHESIS OF KY_3F_{10}:Tm^{3+}

A. Synthesis of powders

The starting fluorides used to synthesize KY_3F_{10}:Tm^{3+} are prepared in the Laboratoire de Chimie de la Matière Condensée de Paris. Yttrium trifluoride is obtained by reaction between its oxide and anhydrous hydrogen fluoride at 800 °C. Potassium fluoride is obtained by reaction between potassium carbonate, K_2CO_3, and an aqueous solution of hydrofluoric acid at 40%. The solution is evaporated at 100 °C until precipitation of KHF_2. The latter is heated, melts at 239 °C, and loses gaseous HF from its melting point to its boiling point at 351 °C.[9] At this temperature solid KF crystallizes. It is hygroscopic and must be protected from moisture in a glove box placed under dry argon. All KY_3F_{10}:Tm^{3+} samples are synthesized by direct solid-state reaction between KF, YF_3, and TmF_3 according to

$$\text{KF} + 3(1-x)\text{YF}_3 + 3x\text{TmF}_3 \rightarrow \text{K}(\text{Y}_{1-x}\text{Tm}_x)_3\text{F}_{10}.$$

The stoichiometric mixture of the starting fluorides is homogenized in the glove box, in a mortar, and introduced in a gold crucible, which is sealed and heated at 880 °C for 24 h.

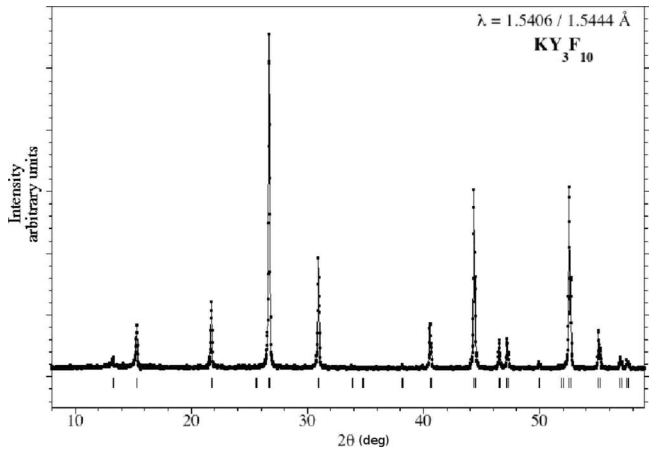

FIG. 2. X-ray powder pattern of KY_3F_{10}. The short vertical lines indicate the positions of the Bragg reflections for a face-centered-cubic cell with a cell parameter of 11.537 Å.

$KY_3F_{10}:Tm^{3+}$ samples obtained by this process are then heated again at the same temperature for 3 h under an anhydrous hydrogen fluoride stream in order to eliminate all traces of oxygen and hydroxyl groups.

The products are characterized by their x-ray powder-diffraction (Fig. 2) patterns recorded on a vertical Philips PW1050/25 goniometer mounted in the Bragg-Brentano configuration $(\theta, 2\theta)$ with a Ni-filtered Cu $K\alpha$ radiation. All the x-ray powder patterns are identical. The diffraction lines can be indexed on the basis of a cubic cell with a space group $Fm3m$ and a refined cell parameter of 11.537(4) Å, in agreement with the crystal structure of KY_3F_{10}.[10] The absence of unindexed diffraction lines indicates that the reaction between the starting fluorides is completed for each sample. No significant variations in the cell parameter as function of the rare-earth rate are detected. This feature can be explained by the radii of the Y^{3+} and Tm^{3+} ions, which are very close, 1.019 and 0.994 Å, respectively.

B. Synthesis of crystals

1. Growth using the micro-pulling-down method

The micro-pulling-down (μ-PD) method was modified for the growth of fluoride crystals.[11] The concept is similar as for oxide compounds. The growth chamber can be evacuated up to 10^{-5} Torr by combined rotary and diffusion pumps. The growth chamber is equipped with a CaF_2 window for visual observation of the solid/liquid interface using a charge-coupled device (CCD) camera with monitor. High-purity graphite crucibles were used and were inductively heated using a radio-frequency generator. Starting materials were prepared from a stoichiometric mixture of 4N, KF, YF_3, and TmF_3 powders (Stella Chemifa Co. Ltd.). They were thoroughly mixed and put into the crucible. The chamber was evacuated to 10^4 Torr and the crucible was heated to 600 °C for 1 h to remove oxygen impurities. During this baking procedure, the chamber is further evacuated up to 10^5 Torr. After the baking, the recipient was filled with high-purity CF_4 (6N) until ambient pressure and the crucible was heated up to the melting temperature of about 1030 °C. Crystal growth was carried out using an a-axis seed of undoped KYF crystal. The growth rate was 0.1–0.15 mm/min. Controlling power and pulling rate during the growth process constantly maintained the crystal diameter.

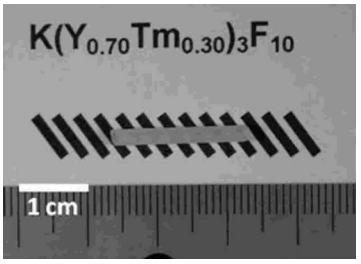

FIG. 3. As-grown $K(Y_{0.3}Tm_{0.7})_3F_{10}$ single crystals.

2. Results

KY_3F_{10} crystallizes in the cubic fluorite-type structure with space group and lattice parameter $a=11.54$ Å. Each trivalent RE dopant ion in a KY_3F_{10} single crystal is surrounded by eight fluorine atoms forming an antiprism $(YF_8)^{5-}$ site, which belongs to C_{4v} site symmetry.[12] KY_3F_{10} is the only compound in the KF-YF_3 system that melts congruently without any phase transition. Moreover, due to its attractive thermomechanical properties, wide transparency, and high optical damage threshold, KY_3F_{10} has been widely studied as solid-state laser material when activated by several RE ions, which can easily substitute for Y^{3+} ions in a noncentrosymmetrical site. In addition, its relatively low phonon energy (500 cm^{-1}) is efficient in avoiding energy loss by nonradiative relaxation. Single crystals of $K(Y_{1-x}Tm_x)_3F_{10}$ $(0.05 \leq x \leq 0.8)$ were successfully grown by the μ-PD method. The grown fluoride crystals were transparent with a slightly white color, which increases with increasing Tm concentration. The rod-shaped crystals were 2.0–2.5 mm in diameter and 20–30 mm in length. Neither visible inclusions nor cracks were observed (Fig. 3). The surface of the crystals was smooth, and the diameter was constant in the steady-state growth region.

3. X-ray characterization

To identify the obtained phase, powder x-ray-diffraction (XRD) analysis was carried out in the 2θ range from 10 to 70 using a Rigaku diffractometer (RINT2000). The x-ray source was Cu $K\alpha$ with accelerating voltage of 40 kV and tube current of 40 mA. All x-ray experiments were carried out at room temperature (RT) under air ambient. The evolution of powder XRD diffractograms is shown in Fig. 4. No impurity phases were detected, and we conclude that $K(Y_{1-x}Tm_x)_3F_{10}$ forms a complete solid solution with high crystallinity compared to Czochralski (Cz) grown ones.

IV. EXPERIMENTAL

The spectrometer allows one to excite phosphors samples in the VUV-UV spectral range; to record the VUV diffuse reflection, covering the $\lambda=110$ nm to $\lambda=240$ nm spectral

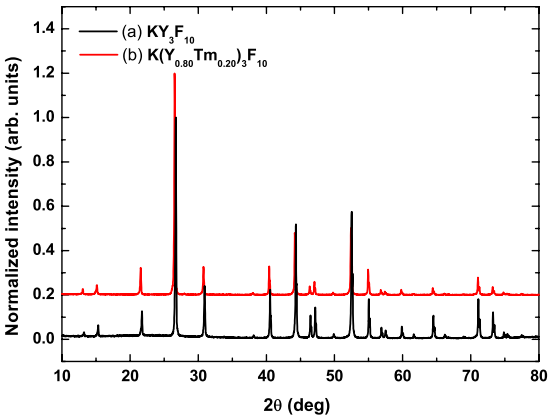

FIG. 4. (Color online) Powder x-ray-diffraction patterns of (a) undoped and (b) $K(Y_{0.8}Tm_{0.2})_3F_{10}$ single crystals.

range; and to analyze the fluorescent emission in the UV visible range. The UV excitation source is a 150 W deuterium lamp equipped with a MgF_2 output window from Hamamatsu. The lamp is directly mounted in front of the monochromator entrance slit with a special vacuum flange. The Beaudouin MVR 100 vacuum monochromator has a focal length of 1 m. Its concave grating is blazed at 800 Å and it has 1200 lines/mm giving a dispersion of 1 nm/mm and resulting in a potential resolution of the system well below 1 Å. It is continuously evacuated by an ATP 150 turbo pump from Alcatel, the pressure being less than 10^{-7} Torr. The sample chamber is directly mounted on the exit slit of the monochromator. Like the excitation source, it can be isolated from the vacuum monochromator by a gate valve. The sample chamber is equipped with its own ATP 80 turbo pump from Alcatel. The sample holder is approximately at 20 cm from the exit slit of the monochromator, such that the size of the light spot on the surface of the sample is about 4 mm wide and 8 mm high. In order to have a reference of VUV intensity, a MgF_2 beam splitter is used to pick up a small percentage of the exciting beam and to deviate it toward a solar-blind photomultiplier tube (PMT) (Hamamatsu R8486). This PMT has been calibrated by Hamamatsu Company and its spectral sensitivity is known. The sample holder can hold five samples at the same time. Small cavities of two-tenths of a millimeter in depth and 1 cm in diameter were engraved to receive the samples. The surface of the sample is positioned perpendicularly to the exciting beam. The detection is arranged in a 45° geometry relative to the excitation axis. On one side the reflected light from the sample is collected by a second solar-blind PMT, and on the other side the emitted light is collected by an optical guide made of a UV-grade quartz rod 2 cm in diameter. This rod guides the light toward one exit window on which a PMT equipped with a filter holder is set. The PMT signal is fed into a single-photon-counting unit. The complete system is driven and controlled by a homemade software on a microcomputer. This set up allows one to record simultaneously the excitation and the diffuse reflection spectra.

The UV excited fluorescence decay curves are recorded with 157 nm F_2 excimer pulsed laser excitation. The pulse energy was 100 μJ and the pulse frequency was 20 Hz. The

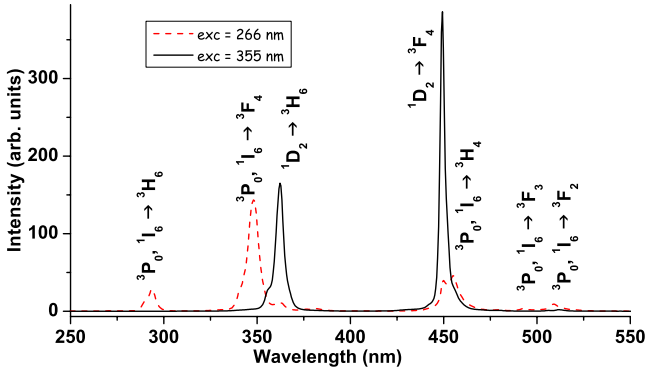

FIG. 5. (Color online) Emission spectra of $KY_3F_{10}:Tm^{3+}5\%$ crystal under 266 nm (dashed curve) and 355 nm (solid curve) laser excitations.

decay curves are directly recorded by feeding the output of the 9789 EMI photomultiplier into one channel of a Lecroy LT oscilloscope or a SR430 multichannel analyzer from Stanford Research.

V. RESULTS AND DISCUSSION

We now discuss the various experiments that provide evidence for quantum cutting. As seen in Fig. 1, quantum cutting would provide new energy relaxation pathways that will enhance the populations of some of the $4f^{13}$ levels. Figure 1 shows one such cross-relaxation pathway that would result in an increase in the $^1D_2$ population. However other channels also likely involve a process that leaves one ion in the $^1I_6$ and ^3P_J manifolds and the other in $^1G_4$. As will be seen below from a discussion of the VUV emission, it appears that the resonance condition described in Fig. 1 is not the dominant CRET pathway based on a consideration of the available resonance conditions for CRET.

A. UV-visible spectroscopy

1. Assignment of the emissions

To assign without any ambiguity the different emission lines to the different emitting levels, we have recorded emission spectra of $KY_3F_{10}:Tm^{3+}5\%$ under 266 and 355 nm laser excitations. The resulting spectra are displayed in Fig. 5. The 355 nm excitation excites selectively the $^1D_2$ level. Under this wavelength of excitation the 293.5, 348.0, 455.0, 492.5, and 509.0 nm emissions are absent, whereas they are present under selective excitation of the $^3P_2$ level (266 nm excitation). So we can deduce that these emissions originate from the $^3P_0(^1I_6)$ level. The two most intense peaks under 355 nm excitation, at 362.5 and 449.5 nm, are also present under 266 nm excitation so they originate from the $^1D_2$ level. (The levels below the $^1D_2$ level cannot be responsible for these emissions because they are at too low energy.)

2. Quenching process

The 5, 10, 20, and 30% Tm^{3+}-doped crystals were excited by a 355 nm laser (selective excitation of the $^1D_2$ level), to see the blue luminescence ($^1D_2 \rightarrow {}^3F_4$ transition, at 449 nm).

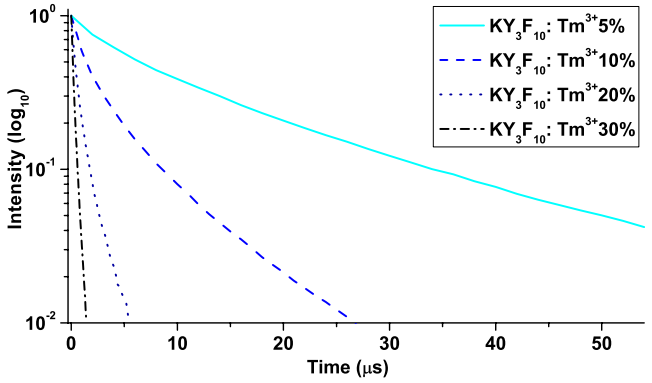

FIG. 6. (Color online) Time-resolved emission of the 449 nm emission of $KY_3F_{10}:Tm^{3+}$, 5, 10, 20, and 30% doped crystals under 355 nm laser excitation.

With the naked eye we have clearly seen that 5% Tm^{3+}-doped material was the most luminescent and that the luminescence intensity decreases when the Tm^{3+} concentration increases. This is consistent with the observation of a cross-relaxation quenching process reported in the literature.[13] The luminescence decays of the different materials are presented in Fig. 6, confirming the existence of blue-luminescence quenching with an increase in Tm^{3+} concentration. The average lifetimes in the 5, 10, 20, and 30% Tm^{3+}-doped crystals are 20, 6, 1.5, and 0.4 μs, respectively. The decays are nonexponential even in the 5% Tm^{3+}-doped sample. Reduction in the fluorescence lifetimes, as well as nonexponentiality of the decays at short times, are indications of cross-relaxation quenching. Indeed, by looking at the energy-level structure of Tm^{3+}, several quasiresonant cross-relaxation pathways may be found such as $(^1D_2, ^3H_6) \rightarrow (^1G_4, ^3H_5)$ or $(^1D_2, ^3H_6) \rightarrow (^3F_2, ^3H_4)$.

3. Temperature effect

Figure 7 depicts the evolution with temperature of the blue-emission spectrum of the $KY_3F_{10}:Tm^{3+}2\%$ powder under 266 nm excitation (selective excitation of the $^3P_2$ level). The blue-emission intensity drastically decreases when the temperature increases. It appears obvious that as the temperature is increased, an additional thermally activated de-

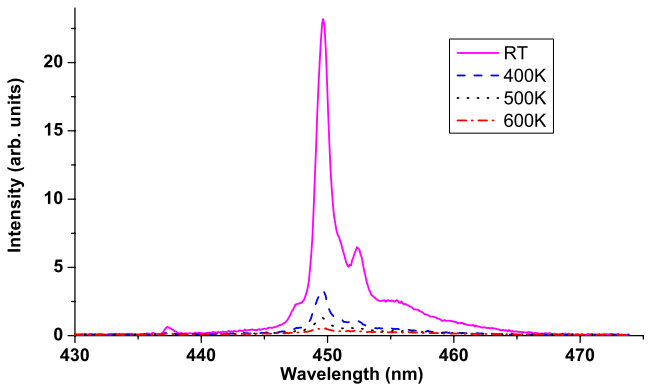

FIG. 7. (Color online) Evolution, with temperature, of $KY_3F_{10}:Tm^{3+}2\%$ powder blue emission, under 266 nm excitation.

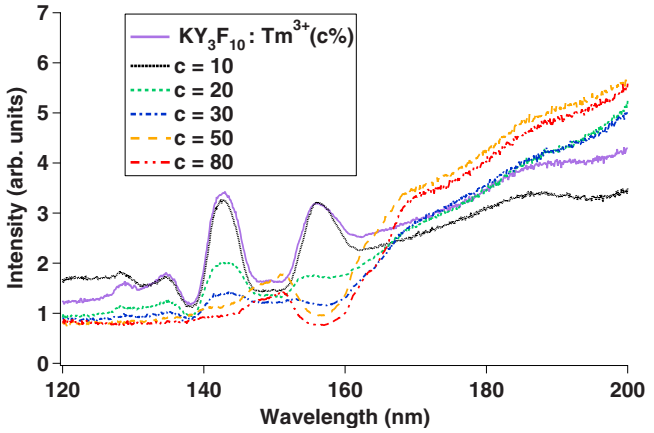

FIG. 8. (Color online) VUV $KY_3F_{10}:Tm^{3+}$ reflection spectra evolution with Tm^{3+} concentration.

excitation pathway occurs that competes with radiative decay. Although luminescence quenching under increased temperature and concentration are both well-known phenomena, it will be seen that the behavior under VUV excitation is totally different.

B. VUV spectroscopy

1. Quenching of VUV Tm^{3+} *emission*

In order to determine the appropriate excitation energies for the 5*d* levels of Tm^{3+}, we first examine the excitation and diffuse reflection spectra. For diffuse reflection one expects to observe a reduction in signal at wavelengths corresponding to the strong 5dLS absorption. The $KY_3F_{10}:Tm^{3+}$ diffuse reflection spectrum obtained for each Tm^{3+} concentration is shown in Fig. 8. The increased diffuse reflection at these 5*d* absorption wavelengths is totally unexpected. Indeed we were anticipating troughs at these absorption energies and plateaus at energies where absorption is absent. Around 160 nm—the wavelength of the first allowed $4f \rightarrow 5d$ transition according to the Dorenbos relationship—we see a trough only for highly doped materials ($KY_3F_{10}:Tm^{3+}50\%$ and 80%). The materials with lowest Tm^{3+} concentration exhibit not a flat zone but rather broad peaks. This unexpected result can be explained when we consider the possibility of VUV emission of these materials. Indeed we know that one of the processes in competition with the cross relaxation involving the 5dHS band of Tm^{3+} is VUV spin-forbidden emission from the 5dHS band. The wavelength of this emission is shifted in comparison to the different excitation wavelengths, which are spin-allowed transitions by the sum of $\Delta E^{Tm^{sa},Tm^{sf}}$ and the Stokes shift $\Delta\text{Stokes}(A)$. However, since there are many more absorbed VUV photons in the material than reflected ones at the strong absorption features, the VUV emission detected by the solar-blind photomultiplier can be greater than the intensity of the reflected light at the surface of the phosphor grains, which represents only a few percent of the total excitation light flux. Furthermore, the spectral sensibility of the Hamamatsu solar-blind PMT is greater at 178 nm (prediction for the spin-forbidden VUV emission) than at 160 nm (wavelengths corresponding to the excitation

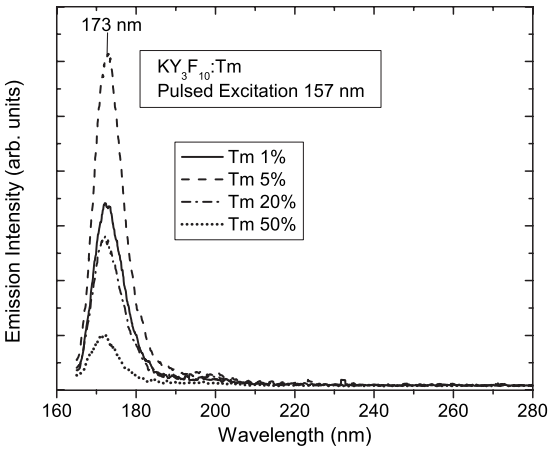

FIG. 9. VUV emission spectra of $KY_3F_{10}:Tm^{3+}$ with different Tm^{3+} concentrations.

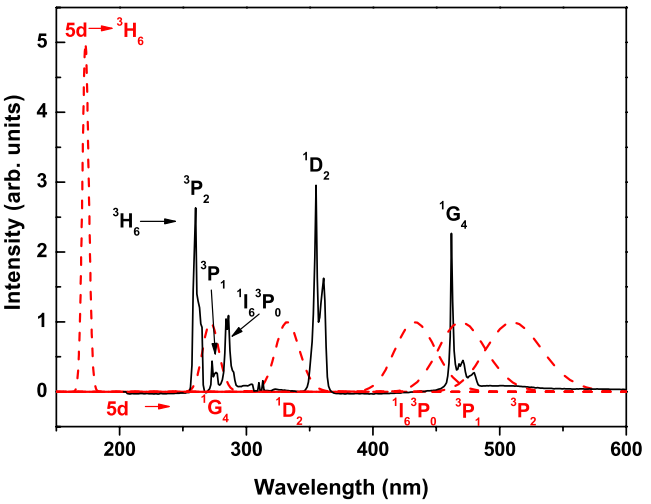

FIG. 10. (Color online) Spectra showing the resonance between $d \rightarrow f$ emission and $f \rightarrow f$ absorption in $KY_3F_{10}:Tm^{3+}$.

transitions, spin allowed). So the observed spectral shape is explained in the following way: for relatively low Tm^{3+} concentrations, $KY_3F_{10}:Tm^{3+}$ mainly emits in the VUV domain under VUV excitation of the $5d$ bands, but for high Tm^{3+} concentrations the VUV emission tends to disappear. This can be explained by the occurrence of the quantum cutting mechanism. It is interesting to note that detection of this quenching using diffuse reflection of Tm^{3+} VUV emission has never been reported before. Papers about materials with Tm^{3+} concentrations of up to 100% do not report any VUV luminescence quenching.[7]

2. *VUV emission spectra of* Tm^{3+}

In order to confirm the presence of VUV emission, emission spectra for a series of samples with different Tm^{3+} concentrations are shown in Fig. 9. The sample is excited with a pulsed excimer laser operating at 157 nm and is detected by a solar-blind PMT after dispersing the emission through a VUV monochromator. Excitation at 157 nm is resonant with the first main feature in the reflection spectra in Fig. 8, which is the lowest 5dLS band. Indeed an emission band peaking at 173 nm is observed along with weaker poorly resolved bands at longer wavelengths. The weaker bands are composed of transitions from both the 5dHS and 5dLS levels to excited multiplets of the $^3H_6$ configuration as has been described previously for $LiYF_4:Tm^{3+}$.[14] The peak at 173 nm is believed to be the 5dHS$\rightarrow{}^3H_6$ transition and is nearby the wavelength predicted by Dorenbos[3] based on Ce^{3+} emission in this host. However there is a significant discrepancy between this prediction and both the observed emission (Fig. 9) and reflection (Fig. 8) peaks. According to the parameters for Ce^{3+}, the main absorption and emission peaks should be at 160 and 178 nm, respectively, rather than the observed values of 157 and 173 nm. The observed values imply a crystal depression energy of $D(A)=14\,940\ \mathrm{cm}^{-1}$, not $16\,084\ \mathrm{cm}^{-1}$ based on Ce^{3+}. The energy difference between the absorption peak and emission peak is however consistent with the Stokes shift obtained from Ce^{3+}. This means that the resonance condition for the CRET creating two ions in the $^1D_2$ state, which ideally required $D(A)=16\,890\ \mathrm{cm}^{-1}$, is not well satisfied. The resulting resonance situation is summarized in Fig. 10. Here the predicted broadband 5dHS emission bands, based on the observed 5dHS$\rightarrow{}^3H_6$ feature [full width at half maximum (FWHM) of 2600 cm^{-1}], are shown along with the absorption spectrum of a sample with 10% Tm^{3+}. One sees that the good resonances expected based on the Ce^{3+} parameters do not occur. As a result, the best resonant condition is one in which the CRET leads to the two Tm^{3+} ions in the $^3P_1$ and $^1G_4$ final states. Other pathways, including the one originally proposed, are nearly resonant and probably also occur so that one can expect populations of the $^1G_4$, $^1D_2$ and the ^3P_J, $^1I_6$ states to result. The VUV emission intensity shown in Fig. 9 increases at first as the Tm^{3+} concentration is raised from 1 to 5%, probably due to the increased absorption, but then continues to decrease as the concentration is further increased. This is consistent with the observation in the reflection spectra that the peaks observed at wavelengths corresponding to the 5dLS-allowed absorption become troughs as the contribution to the total signal from the emission decreases. At high concentration the diffusive reflection signal dominates.

3. *Behavior of the blue emission with* Tm^{3+} *concentration*

Evidence for quantum cutting can be obtained from the excitation spectra detecting the $^1D_2$ blue emission at 449.5 nm in samples of $KY_3F_{10}:Tm^{3+}$ with different Tm^{3+} concentrations. It can be seen in Fig. 11 that the excitation peak at 157 nm is stronger for the sample with 10% Tm^{3+} than for the one with 5%. It then decreases for concentrations higher than 20%. This observation is totally consistent with the quantum cutting mechanism described in Fig. 1: for Tm^{3+} concentrations higher than 5%, the CRET depopulating the $5d$ band to the benefit of the $^1D_2$ blue-emitting level allows the increase in the blue-luminescence intensity. But even if this process continues to increase with Tm^{3+} concentration (decreasing the VUV emission intensity), the quenching phenomenon of the blue-emitting levels, seen before, becomes very important too and the blue luminescence decreases at higher concentrations.

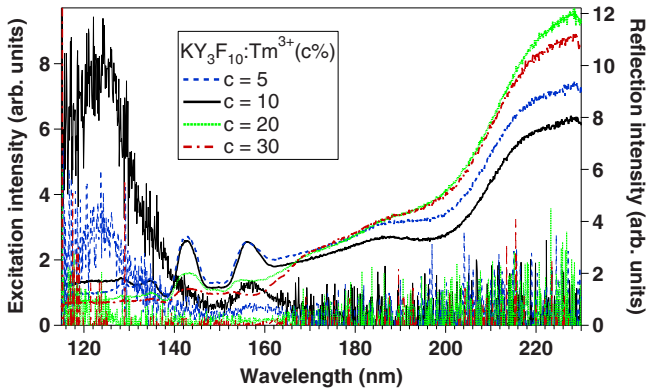

FIG. 11. (Color online) VUV excitation (detection 450 nm) and diffuse reflection spectra of $KY_3F_{10}:Tm^{3+}$ with different Tm^{3+} concentrations.

4. Temperature dependence

Seeking to favor the cross-relaxation mechanism relative to that of the VUV emission from the bottom of the 5dHS band, we performed a study as function of temperature. The temperature dependence of the $KY_3F_{10}:Tm^{3+}10\%$ excitation and diffuse reflection spectra is depicted in Fig. 12. Diffuse reflection spectra (dotted lines) show a similar behavior as a function of an increase in temperature as that observed with an increase in Tm^{3+} concentration: it follows that the VUV emission is quenched when the temperature is increased. As seen from a comparison with the excitation spectra in Fig. 12, the quenching of the VUV emission is accompanied by an increase in the blue luminescence. This behavior occurs for all other Tm^{3+} concentrations that were studied and is therefore a different process from the CRET that leads to quantum cutting. To understand this blue-luminescence increase, consider the $KY_3F_{10}:Tm^{3+}2\%$ emission-spectrum evolution with temperature, shown in Fig. 13. An intensity increase is seen for all UV visible emissions with temperature, but transitions from the $^3P_0$ level undergo a stronger increase. Indeed, whereas the $^3P_0 \rightarrow {}^3F_4$ and $^1D_2 \rightarrow {}^3H_6$ transitions' intensities are similar at room temperature, at 600 K the intensity of the transition from the $^3P_0$ level is more than twice that of the intensity of the transition from the $^1D_2$ level. Whereas under VUV excitation there was a relative enhancement of the population of the $^1D_2$ level (in comparison to the $^3P_0$ level), the reverse tendency occurs with a temperature increase. This phenomenon is explained in the following way. Whereas at room temperature in the $KY_3F_{10}:Tm^{3+}2\%$ sample, VUV emission remains the dominant process under VUV excitation (quantum cutting by CRET is weak at these low Tm^{3+} concentrations), the temperature increase enables a very efficient auxiliary depopulation pathway from the $5d$ band. The phenomenon which is responsible for that is probably the transfer of the energy from the $5d$ band to the lower $4f$ levels ($^3P_2$, $^3P_1$, $^3P_0$, and $^1I_6$) via an intersystem crossing that is thermally activated. This phenomenon becomes more efficient at higher temperatures.

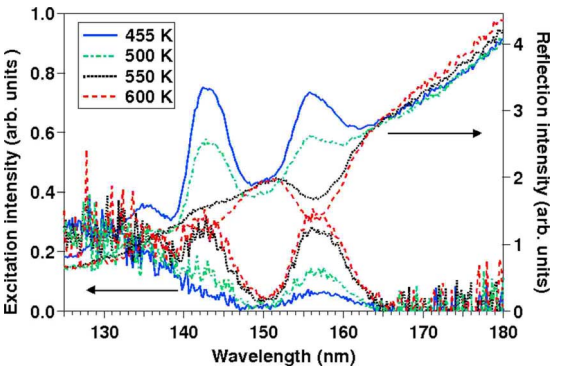

FIG. 12. (Color online) Excitation (detection 450 nm) and diffuse reflection spectra of $KY_3F_{10}:Tm^{3+}10\%$ depending on temperature.

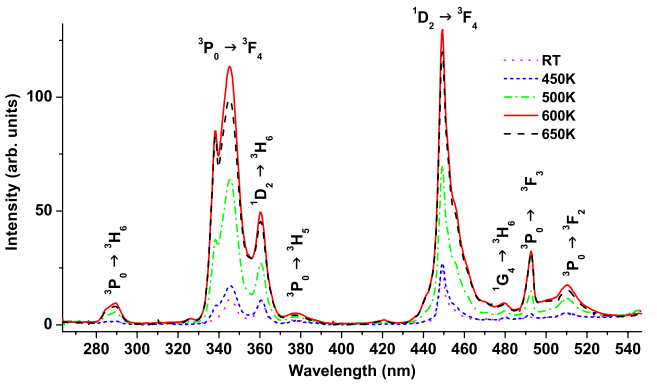

FIG. 13. (Color online) Emission spectra of $KY_3F_{10}:Tm^{3+}2\%$ powder evolution with temperature for excitation at 157 nm.

VI. TIME-RESOLVED STUDY OF THE QUANTUM CUTTING

In order to gain a better understanding of the quantum cutting process and provide additional evidence for its occurrence, time-resolved studies were performed of the decay of the $5d$ state and buildup of the states of the $4f^{13}$ configuration. Data obtained at 300 K on samples of $KY_3F_{10}:Tm^{3+}$ containing 1, 5, 20, and 50% of Tm^{3+} are shown in Fig. 14. The samples are excited at 157 nm with a pulsed excimer laser. Time-resolved luminescence is detected at 173 nm with a solar-blind PMT, corresponding to emission from the 5dHS state and at 363 nm to monitor the $^1D_2$ population. The decay of the 5dHS state exhibits two main features. First, the decay becomes strongly nonexponential as the Tm^{3+} concentration is increased, as especially evident for the sample with a 20% concentration. Second, the decay of the 5dHS state shows a rapid increase in rate with Tm^{3+} concentration. Both of these observations support the proposed CRET mechanism for producing quantum cutting. One expects a strongly concentration-dependent decay rate for the 5dHS state as the process requires a pair of nearby Tm^{3+} ions. The probability that one Tm^{3+} has another Tm^{3+} at some nearby site grows linearly with concentration. The nonexponential behavior is also expected since there is a distribution of pairs. Some Tm^{3+} are well separated from other Tm^{3+} ions such that their relaxation is similar to that of a single ion. Other Tm^{3+} may

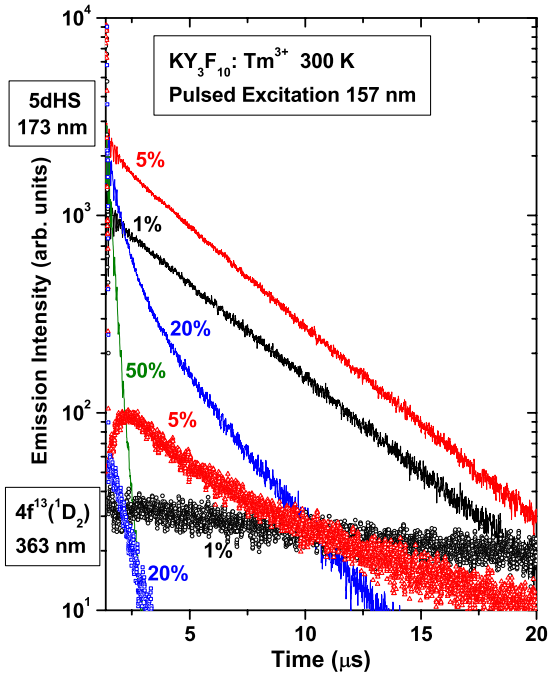

FIG. 14. (Color online) Decay times of VUV and UV emissions of KY_3F_{10}:Tm^{3+} with different Tm^{3+} concentrations.

have one or more nearby Tm^{3+} neighbors such that relaxation is dominated by the fast CRET. The result of considering an ensemble of all possible pair configurations, each with a different CRET rate, will lead to a nonexponential decay.

The emission from the $^1D_2$ state at 363 nm should show a buildup on a time scale corresponding to the early part of the 5dHS decay since the enhanced decay rate at early times arises from Tm^{3+} ions that have nearby neighbors such that CRET is dominant. The time dependence of the 363 nm emission for different Tm^{3+} concentrations is also seen in Fig. 15. The 5% Tm^{3+} sample shows a distinct buildup in the first 1 or 2 μs. This is the time period where the 5dHS decay at 173 nm shows an initial more rapid decay. The nonexponential decay supports the supposition that CRET is an important relaxation channel for the $^1D_2$ state. The 20% sample exhibits the suggestion of a plateau or slower decay at early times but a much faster decay at longer times. This can be understood as follows. The CRET feeding of the $^1D_2$ state is now very fast, as indicated by the more rapid decay in the early portion of the 5dHS decay. At this high Tm^{3+} concentration, subsequent CRET from the $^1D_2$ state, which is well known for Tm^{3+}, brings down its population so rapidly that the buildup cannot be observed within the time resolution of these experiments. The slower decay at early times results from the fact that the $^1D_2$ state is being fed by the CRET from 5dHS at the same time that it is decaying. A numerical analysis based on a model for the dynamics is presented in Sec. VII which confirms these qualitative statements. The dynamics of the 50% sample is so fast that it is not possible to study the $^1D_2$ population dynamics. The time dependence of the emission in the 1% Tm^{3+} sample shows predominantly an exponential decay. The source of the population is not clear, but it is possible that the thermally activated relaxation from the 5dHS state is still weakly active at 300 K. The dynamics of the emission from $^3P_0(^1I_6)$ at 348 nm exhibits an almost identical behavior.

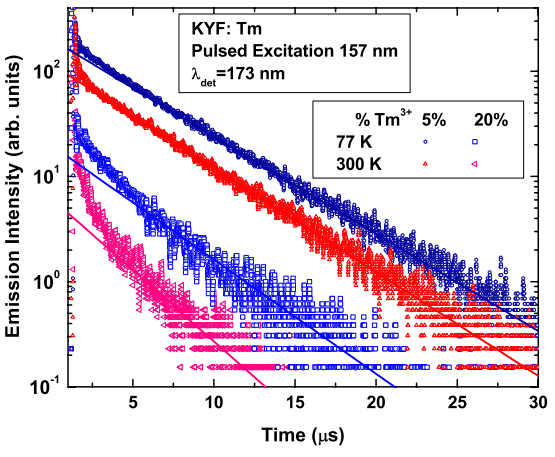

FIG. 15. (Color online) The time dependence of the 173 nm emission, excited at 157 nm, of KY_3F_{10}:Tm^{3+} for temperatures of 77 and 300 K.

The decay of the 5dHS emission at long times is only weakly dependent on Tm^{3+} concentration. This portion of the decay describes the decay of Tm^{3+} ions that are relatively isolated; i.e., their dynamics is characterized by that of single ions. Their decay is therefore dominated by radiative decay and the thermally activated relaxation, discussed earlier, both of which should lead to exponential decays and should be concentration independent. The fact that the decay becomes strongly nonexponential and that this early dynamics is strongly dependent on Tm^{3+} concentration points strongly to the role of CRET and quantum cutting as the cause for the nonexponential behavior.

The role of the thermally activated relaxation occurring via intersystem crossing can be examined from the temperature dependence of the 5dHS dynamics which is shown in Fig. 15. The time dependence of the 173 nm emission, excited at 157 nm, is shown for temperatures of 77 and 300 K. Two main features are seen in this figure. First, the long tails which represent the decay of single ions are nearly independent of temperature, ruling out an important role for the thermally activated relaxation process below 300 K. Second, the initial fast component of the nonexponential decay is somewhat temperature dependent, indicating that the CRET process shows a weak temperature dependence; its rate increases at higher temperatures. This temperature dependence might arise from thermally induced broadening of the transitions which may lead to an improvement in the resonance conditions required for CRET.

VII. CALCULATION OF THE DYNAMICS

With a basic understanding of the processes which control the dynamics of the populations of the Tm^{3+} levels due to cross relaxation, we now model the dynamical behavior to confirm our understanding and to determine the parameters which control the dynamics. The rate equations for the populations of the different levels will be solved under the fol-

lowing features and assumptions. In the following calculation, higher-order cooperative three-body processes such as those described by Dexter[15] are not considered although the same resonant conditions apply as for the two-ion processes considered below. As pointed out by Auzel[16] these are 3–4 orders of magnitude weaker than first-order processes. Although Vergeer *et al.*[17] convincingly demonstrated their existence for $Tb^{3+}(^5D_4) \rightarrow 2Yb^{3+}(^2F_{5/2})$ energy transfer, the transfer rates are only 0.26 ms^{-1}, 3 orders of magnitude less than the CRET rates observed in $KY_3F_{10}:Tm$, and were only observed because there are no possible two-ion processes that could lead to $Tb^{3+}(^5D_4) \rightarrow Yb^{3+}(^2F_{5/2})$ transfer:

(a) The VUV excitation rapidly produces population in the lowest $5d$ state of Tm^{3+}, which is the high-spin (HS) state. At room temperature and below, there is no population in the low-spin (LS) state 2350 cm^{-1} at high energy.

(b) The $5d$ state relaxes by both radiative decay at a rate τ_{5d}^{-1} and by a cross-relaxation pair process. For an excited Tm^{3+} that has one or more nearest-neighbor sites occupied by another Tm^{3+} in its ground state, we define an independent CRET rate. This is justified because for nearest-neighbor pairs an additional exchange contribution to the CRET rate is expected. This results from overlap of the wave functions of a pair of nearest-neighbor Tm^{3+} with an intervening F^-, referred to as superexchange. Even in the absence of exchange, this seems appropriate because the Inokuti-Hirayama model is meant to describe a continuum of nearest-neighbor pair distances, and this breaks down at high concentrations where the local structure is far from continuous. In the case of KY_3F_{10} the local environment contains eight nearest neighbors at 4.03 Å and six next-nearest neighbors at 5.7 Å. The dipole-dipole interactions of the latter is only 12.5% of that of the former, justifying limiting the local structure effects to the eight nearest neighbors. The next group of neighbors consists of 24 at 6.98 Å, where the dipole-dipole interactions are only 3.7% of that of the nearest neighbors. The nearest-neighbor contribution to the rate of decay of the excited Tm^{3+} occurs at a rate j times the rate for a single nearest neighbor, WCR_{5d}, where j describes the number of the eight nearest-neighbor sites that are occupied by a Tm^{3+}:

(a) The dipole-dipole contribution occurs at a rate described by the parameter D, whose magnitude is directly proportional to the Tm^{3+} concentration. It is described here according to the Inokuti-Hirayama formalism, in which the population decays according to

$$N(t) = N(0)\exp[-D(t/\tau)^{1/2} - t/\tau]. \quad (5)$$

(b) The populations of the $^1D_2$ and/or $^1I_6$, $^3P_0$ states of the $4f^{13}$ configuration are fed by the CRET from $5d$. These decay, as does the $5d$ population, by radiative transitions and by both exchange-mediated CRET at a rate WCR_{4f} and dipole-dipole CRET described by the parameter D_{4f}. Since their dynamical behaviors are very similar, we just treat the $^1D_2$ case.

(c) The rate equations are solved independently for each configuration of the number of nearest-neighbor Tm^{3+}. The resulting time-dependent luminescence is calculated by summing the contribution for each of these configurations in proportion to the statistical probability (assumed to be random) that that number of nearest-neighbor positions will be occupied at the actual Tm^{3+} concentration.

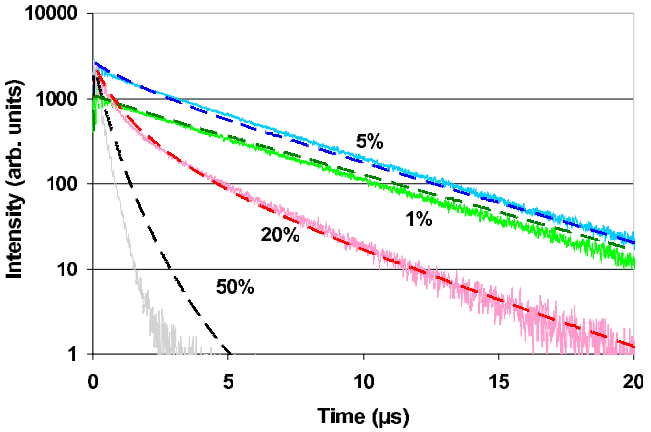

FIG. 16. (Color online) Fits of the decay time of the 173 nm emission, excited at 157 nm, of $KY_3F_{10}:Tm^{3+}$ at 300 K.

(d) For excited Tm^{3+} sites with no nearest-neighbor sites occupied by another Tm^{3+}, we assume only a dipole-dipole CRET. For these, the $5d$ state decays by radiative and dipole-dipole CRETs whose sum determines the rate of feeding of the $4f$ states. The $4f$ states decay by radiative and dipole-dipole CRETs.

(d) The dynamics is treated considering a static model where energy migration among the Tm^{3+} is absent. This assumption can be supported by the fact that the overlap of the $5d$ emission with the $^3H_6$ ground state is very poorly resonant with the corresponding absorption because of the Stokes shift of the $4f \rightarrow 5d$ transition. This may become questionable at the higher Tm^{3+} concentrations, but incorporating migration is beyond the scope of these calculations.

The resulting rate equations for the $5d$ population of a Tm^{3+}, $N_{5d}(j)$, with j nearest-neighbor Tm^{3+}, and the corresponding $4f$ state populations, $N_{4f}(j)$, are

$$dN_{5d}(j)/dt = -[(1/2)D_{5d}(t\tau_{5d})^{-1/2} + \tau_{5d}^{-1} + j(\mathrm{WCR}_{5d})]N_{5d}(j), \quad (6)$$

$$dN_{4f}(j)/dt = dN_{5d}(j)/dt - [(1/2)D_{4f}(t\tau_{4f})^{-1/2} + \tau_{4f}^{-1} + j(\mathrm{WCR}_{4f})]N_{4f}(j). \quad (7)$$

The rate equations for each j are solved in a self-consistent manner as a function of Tm concentration. The values of τ_{5d} and τ_{4f} are obtained from the decays of the 1% Tm samples and are fixed throughout the calculation. WCR_{5d} and WCR_{4f} are varied in the attempt to find a best fit but they are held constant as a function of Tm concentration for a fit to the series of concentrations. D_{5d} and D_{4f} are varied in the fitting but their value is taken to be linear in Tm concentration in fitting the series of concentrations. The total $5d$ and $4f$ populations are obtained as a sum of the populations for all $j = 0-8$ according to the statistical probability of finding each j configuration at that concentration.

The results are shown in Fig. 16 for the $5d$ emission. The fits are quite good but the calculations underestimate the de-

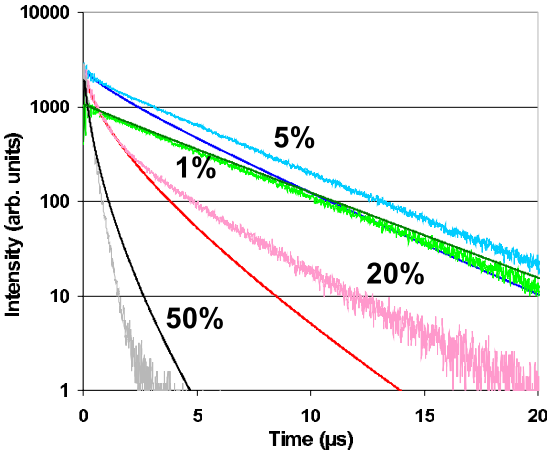

FIG. 17. (Color online) Fits of the decay time of the 173 nm emission, excited at 157 nm, of $KY_3F_{10}:Tm^{3+}$ at 300 K using only dipole-dipole interactions.

cay rate of the 50% sample. The neglect of migration is probably partly responsible. It is not possible to obtain good fits using only dipole-dipole interactions as shown in Fig. 17, where the dipole-dipole parameters were chosen to fit the early time dependence. One sees that it is not possible to describe the strongly nonexponential behavior of the data. In general, energy migration will lead to a more exponential not less exponential behavior, thus our belief that the nearest neighbors must be treated separately in describing the CRET. This is true regardless of whether the exchange is active for the nearest-neighbor Tm ions since the Inokuti-Hirayama model does not consider the local structure. The behavior of the $4f$ emission is shown in Fig. 18. For the $4f$ dynamics, an additional variable is introduced to take account of the relative contribution of the $j=0$ configuration. This is necessary because the relative amount of feeding of the various $4f$ states for the radiative decay, $5d \rightarrow 4f$, may be quite different from that for the dipole-dipole feeding. This is only important for the 1% and 5% samples since the $j=0$ configuration

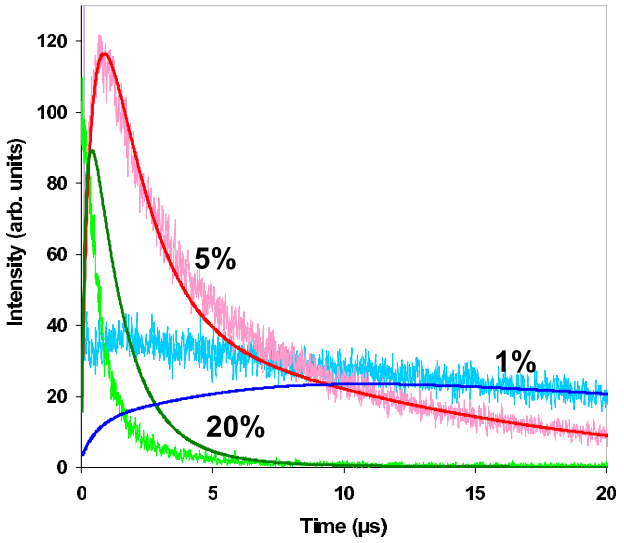

FIG. 18. (Color online) Fits of the time dependence of the 363 nm emission, excited at 157 nm, of $KY_3F_{10}:Tm^{3+}$ at 300 K.

TABLE II. Parameters in the model for fitting the time-dependent emission.

	$5d$	$4f$
τ (μs)	5	40
D [a]	$0.05C$	$1.0C$
R_0 (nm)	0.345	0.94 (0.9 $^1D_2$ in YAG[b])
P_{SA}^{dd} (10^6 s^{-1}) experiment	0.081	4.2
P_{SA}^{dd} (10^6 s^{-1}) calculation	0.05[c]	
WCR (10^6 s^{-1})	0.4	1.4

[a] C is the concentration in percent Tm^{3+}.
[b] Reference 13.
[c] Estimated based on discussion in text for CRET $(5dHS, {}^3H_6) \rightarrow ({}^3P_1, {}^1G_4)$.

has a very small probability at 20% Tm and greater. The decay of the $4f$ emission of the 5% Tm sample is described very well. Both the buildup and decay rates of the 20% Tm sample are underestimated. Energy migration is likely the explanation since the excitation initially prepared on a low-j site can migrate to a site with larger j where it can decay more quickly. The 1% sample shows a component with a much faster rise time than predicted, which suggests that there are other nonradiative processes that become relatively important as the CRET rates get rather slow. We have not shown or attempted to describe the $4f$ dynamics of the 50% samples as it is beyond our experimental time resolution.

The parameters which were used in the model are summarized in Table II. The dipole-dipole parameter for the $5d$ state is $0.05C$, where C is the concentration in percent Tm^{3+}. From this it is possible to calculate the critical distance for which the dipole-dipole CRET rate is equal to the radiative rate. For the CRET from the $5d$ state, this is 0.345 nm. From this the nearest-neighbor dipole-dipole transfer rate is found to be 0.081×10^6 s^{-1}. This is about 20% of the total nearest-neighbor rate used in the fitting and about 40% of the radiative rate. This implies that the nearest-neighbor CRET is dominated by exchange interactions. For the CRET leading to quenching of the $4f^{13}$ emission, the situation is quite different. The critical radius obtained from the fit is about 0.94 nm, similar to the value found in yttrium aluminum garnet (YAG).[13] The nearest-neighbor dipole-dipole rate is then 4.2×10^6 s^{-1}, approximately three times larger than the nearest-neighbor rate obtained from the fit to the data. This is opposite to the behavior for the $5d$ state and suggests that the exchange is much less important for the $4f$ state.

It is interesting to try to estimate the dipole-dipole nearest-neighbor rate for the CRET from the $5d$ state and compare it with the observed rates. This can be done using estimates for the oscillator strengths for the $5d \rightarrow 4f$ and the $4f \rightarrow 4f$ transitions. Using the CRET path with the most favorable overlap, we estimate, based on numbers from Tm^{3+} in $YiLiF_4$,[18] that the oscillator strength for the ${}^3H_6 \rightarrow {}^1G_4$ transition is $f_S = 2 \times 10^{-6}$. For the $5dHS \rightarrow {}^3P_1$ transition, we can only make a crude estimate since this emission is too weak and broad to observe. We know that the radiative lifetime of the 5dHS state, for which all transitions are spin forbidden, is 5 μs. From this we can estimate a total oscil-

lator strength including all transitions to be about 2×10^{-4}. If 2% of the oscillator strength falls in the $5d\rightarrow{}^3P_2$ transition, then the oscillator strength is about $f_A=4\times10^{-6}$. The spectral overlap of a broad transition and sharp transition is given by 1/width of the broad transition or about $S_{SA}=3\times10^{-4}$ cm^{-1}. Using the expression[19]

$$P_{SA}^{dd}=1.4\times10^{24}f_S f_A S_{SA}/\Delta E^2 R_{SA}^6, \tag{8}$$

where R_{SA} is in angstroms and $\Delta E=3$ eV, one estimates a value of $P_{SA}^{dd}\approx5\times10^4$ s^{-1}, almost a factor of 2 less than obtained in the experiment. However this includes only the $(5dHS,{}^3H_6)\rightarrow({}^3P_1,{}^1G_4)$ CRET pathway. If one then adds the also strongly resonant $(5dHS,{}^3H_6)\rightarrow({}^1G_4,{}^3P_1)$ channel and the channels involving a final state with both ions in the ${}^1D_2$ state (more poorly resonant), the agreement is quite reasonable.

Unfortunately, one sees that both the dipole-dipole and exchange rates only become competitive with the radiative rate of the $5d$ state for the nearest-neighbor pairs. In this circumstance, one is forced to work at very high dopant concentrations. For Tm^{3+} this leads to very strong quenching of the $4f^{13}$ states responsible of the desired blue luminescence.

VIII. CONCLUSION

In order to find an efficient blue phosphor under VUV excitation, we have synthesized KY_3F_{10} doped with Tm^{3+} as polycrystalline powders and single crystals. Theoretical calculations showed that the position of $5d$ bands of Tm^{3+} in this material lies at a suitable energy in order to induce an effective down-conversion to the ${}^1D_2$ level, leading to the emission of two blue photons for each VUV photon absorbed. However, measurements of the luminescence showed that the actual CRET resonance conditions were significantly different from those predicted by the Dorenbos equation using the previously derived parameters for Ce^{3+} in this host so that the CRET rates for quantum cutting may actually favor population of the ${}^3P_1$ and ${}^1G_4$. The efficiency of this quantum cutting process has been studied as a function of temperature and Tm^{3+} concentration. We have shown that for Tm^{3+} concentrations of 5% or more, the CRET down-conversion process effectively VUV competes with the $5d$ radiative emission but that at these higher concentrations cross-relaxation and nonradiative transitions to lower infrared levels induce quenching of the blue emission. Nevertheless quantum cutting is clearly demonstrated after excitation of the $5d$ state for Tm^{3+} concentrations above 5% in KY_3F_{10}. The time-resolved study of 5dHS and $4f^{13}$ emissions under 157 nm excitation supports the fact that CRET is an important relaxation channel for feeding the ${}^3P_1$ and ${}^1D_2$ states. A model that treats explicitly the nearest-neighbor interactions separately from the ensemble averaged dipole-dipole interactions leads to the conclusion that the exchange interaction plays the dominant role in the nearest-neighbor CRET involving the $5d\rightarrow4f$ process. It is possible that other hosts which satisfy the resonance conditions even more favorably would allow CRET from the $5d$ state at lower Tm^{3+} concentrations, thereby reducing the quenching of the blue luminescence and increasing the visible quantum yield. However, it appears that while this system is very interesting for understanding the process of CRET from the $5d$ state, a process involving CRET from the $5d$ state using a pair of Tm^{3+} is not likely to lead to a commercial VUV excited quantum cutting phosphor.

ACKNOWLEDGMENTS

A.J. acknowledges Akira Yoshikawa for fruitful discussions during the single crystals' preparation. The authors thank Richard Moncorgé for having provided them with a single crystal of KY_3F_{10} doped with Tm^{3+}.

*lena.beauzamy@gmail.com
†moine@pcml.univ-lyon1.fr
‡rmeltzer@physast.uga.edu
§yizhou@physast.uga.edu
‖gredin@upmc.fr
¶drjouinianis@yahoo.fr
**kjiny72@tagen.tohoku.ac.jp

[1] G. H. Dieke, *Spectra and Energy Levels of Rare Earth Ions in Crystals* (Interscience, New York, 1968).
[2] R. T. Wegh, A. Meijerink, R. J. Lamminmaki, and J. Holsa, J. Lumin. **87-89**, 1002 (2000).
[3] P. Dorenbos, J. Lumin. **91**, 155 (2000).
[4] R. T. Wegh, Ph.D. thesis, Utrecht University, 1999, Chap. 5.
[5] J. Y. Gesland, N. M. Khaidukov, N. Y. Kirikova, M. Kirm, J. C. Krupa, V. N. Makhov, T. V. Ouvarova, M. Queffelec, and G. Zimmerer, J. Electron Spectrosc. Relat. Phenom. **101-103**, 579 (1999).
[6] M. True, M. Kirm, E. Negodine, S. Vielhauer, and G. Zimmerer, J. Alloys Compd. **374**, 36 (2004).
[7] V. N. Makhov, N. M. Khaidukov, D. Lo, J. C. Krupa, M. Kirm, and E. Negodin, Opt. Mater. (Amsterdam, Neth.) **27**, 1131 (2005).
[8] M. True, Y. Chen, M. Kirm, S. Vielhauer, and G. Zimmerer, J. Lumin. **124**, 279 (2007).
[9] A. Pierrard, P. Gredin, and A. de Kozak, Powder Diffr. **11**, 121 (1996).
[10] A. Grzechnik, J. Nuss, K. Friese, J.-Y. Gesland, and M. Jansen, Z. Kristallogr. - New Cryst. Struct. **217**, 460 (2002).
[11] K. J. Kim, A. Jouini, A. Yoshikawa, R. Simura, G. Boulon, and T. Fukuda, J. Cryst. Growth **299**, 171 (2007).
[12] A. Ayala, M. Oliveira, J. Gesland, and R. Moreira, J. Phys.: Condens. Matter **10**, 5161 (1998).
[13] S. Guy, M. Malinowski, Z. Frukacz, M. F. Joubert, and B. Jacquier, J. Lumin. **68**, 115 (1996).
[14] R. T. Wegh and A. Meijerink, Phys. Rev. B **60**, 10820 (1999).
[15] D. Dexter, Phys. Rev. **108**, 630 (1957).
[16] F. Auzel, Chem. Rev. (Washington, D.C.) **104**, 139 (2004).
[17] P. Vergeer, T. J. H. Vlugt, M. H. F. Kox, M. I. den Hertog, J. P. J. M. van der Eerden, and A. Meijerink, Phys. Rev. B **71**, 014119 (2005).
[18] Y. Lu, Y. Dai, J. Wang, Y. Yang, Q. Dong, S. Li, and B. Sun, Opt. Commun. **273**, 182 (2007).
[19] T. Kushida, J. Phys. Soc. Jpn. **34**, 1318 (1973).